Momentum Transport in Organized Shallow Cumulus Convection

Savazzi, Alessandro C.M.; Nuijens, Louise; De Rooy, Wim; Janssens, Martin; Siebesma, A. Pier

Important note
To cite this publication, please use the final published version (if applicable).
Please check the document version above.

Momentum Transport in Organized Shallow Cumulus Convection

ALESSANDRO C. M. SAVAZZI,[a] LOUISE NUIJENS,[a] WIM DE ROOY,[b] MARTIN JANSSENS,[a,c]
AND A. PIER SIEBESMA[a,b]

[a] *Delft University of Technology, Delft, Netherlands*
[b] *Royal Netherlands Meteorological Institute (KNMI), De Bilt, Netherlands*
[c] *Wageningen University and Research, University in Wageningen, Wageningen, Netherlands*

ABSTRACT: This study investigates momentum transport in shallow cumulus clouds as simulated with the Dutch Atmospheric Large Eddy Simulation (DALES) for a 150×150 km^2 domain east of Barbados during 9 days of EUREC^{4}A. DALES is initialized and forced with the mesoscale weather model HARMONIE–AROME and subjectively reproduces observed cloud patterns. This study examines the evolution of momentum transport, which scales contribute to it, and how they modulate the trade winds. Daily-mean momentum flux profiles show downgradient zonal momentum transport in the subcloud layer, which turns countergradient in the cloud layer. The meridional momentum transport is nontrivial, with mostly downgradient transport throughout the trade wind layer except near the top of the surface layer and near cloud tops. Substantial spatial and temporal heterogeneity in momentum flux is observed with much stronger tendencies imposed in areas of organized convection. The study finds that while scales < 2 km dominate momentum flux at 200 m in unorganized fields, submesoscales $\mathcal{O}(2–20)$ km carry up to 50% of the zonal momentum flux in the cloud layer in organized fields. For the meridional momentum flux, this fraction is even larger near the surface and in the subcloud layer. The scale dependence of the momentum flux is not explained by changes in convective or boundary layer depth. Instead, the results suggest the importance of spatial heterogeneity, increasing horizontal length scales, and countergradient transport in the presence of organized convection.

KEYWORDS: Subtropics; Convective-scale processes; Mesoscale processes; Momentum; Convective parameterization; Large eddy simulations

1. Introduction

Shallow cumulus clouds cover vast areas over the tropical and subtropical oceans. They influence the atmosphere through their effect on the humidity and temperature distribution (Tiedtke 1989; Neggers et al. 2007), and through their modulation of the radiation budget (Bony et al. 2020). Shallow convection precipitates and organizes frequently, which may matter for the energy budget and the momentum budget in ways that are not well understood. In recent years, mesoscale organization has drawn increased attention from the community. The main focus has been on describing and explaining mesoscale patterns in clouds. Studies have also emphasized the presence of cold pools and gustiness at times of significant precipitation (Vogel et al. 2021; Vial et al. 2019; Zuidema et al. 2017) and the ubiquity of shallow mesoscale overturning circulations (SMOCs) on scales of 10–100 km (George et al. 2021a).

This study focuses on momentum transport in shallow cumulus fields with different mesoscale organization. Convective momentum transport by shallow cumulus (shallow CMT in short) has been studied primarily in the context of idealized cloud cases, such as BOMEX (Brown 1999; Larson et al. 2019) and RICO (Schlemmer et al. 2017), which do not represent the widely varying cloud and wind fields observed in nature. It has hardly been evaluated to what extent such realistic and complex cloud fields further complicate known issues with representing momentum fluxes in models. In general, common approaches to model turbulent and convective fluxes require scrutiny, as model grid spacings are approaching the scales of convection.

The mass-flux approach is commonly used for convective transport of heat and moisture, and also often of momentum. CMT parameterizations of deep convection (e.g., Kershaw and Gregory 1997) combine the convective mass flux with an empirical relationship that relates the cross-updraft pressure gradient to the large-scale vertical wind shear, while others (Schneider and Lindzen 1976) assume the updraft or downdraft have horizontally uniform properties. In the context of deep convection, Badlan et al. (2017) shows how these schemes are not able to represent the transport associated with organized mesoscale circulations, as they neglect an important mesoscale pressure gradient term in the momentum budget. Models handle the transport of momentum by shallow convection in ways that are not readily documented. A variety of approaches appear in place, that include transport in the cloud layer by a mass-flux scheme, an eddy-diffusivity

mass-flux (EDMF) approach, which also includes a dry mass flux of momentum in the subcloud layer, or higher-order turbulence schemes, which include prognostic equations for the variance and fluxes.

Larson et al. (2019), and also Helfer et al. (2021) and Dixit et al. (2021), highlight the complex layered structure of wind and momentum flux in typical shallow convective boundary layers, whereby the zonal wind establishes a jet or local maximum near cloud base. This implies that buoyant updrafts can carry slower momentum originating from the surface upward through cloud base into the lower cloud layer, which results in countergradient transport: an enhancement of the vertical gradient of the wind. To model the significant transport that results from smaller dry plumes (subcloud layer overturning), an eddy-diffusivity approach in the subcloud layer alone would not be sufficient. In the cloud layer, the environmental wind decreases with height, so that the momentum deficit in those updrafts will turn into a momentum excess somewhere in the cloud layer, above which the transport becomes downgradient again.

Already demonstrated by Brown (1999) and Schlemmer et al. (2017), the mass-flux approach underestimates momentum fluxes in the cloud layer to a greater degree than it underestimates moisture and heat fluxes. Part of the missing flux is attributed to environmental velocity fluctuations that may be produced through pressure perturbations created by cloud cores. Compared to BOMEX simulations in Larson et al. (2019), the countergradient transport layer is notably more pronounced and deeper in double-nested LES with time-varying forcing run with ICON on 100×100 km^2 domains (based on the NARVAL campaigns) (Helfer et al. 2021; Dixit et al. 2021). In the ICON-LES hindcasts, a varying large-scale forcing and the use of open boundaries likely favored the development of a larger variety of (deeper) shallow convective systems with more pronounced horizontal circulations. Dixit et al. (2021) analyzed the budget of the momentum flux in these simulations, which revealed that the dominant mechanism acts through a subtle balance between the flux generation through nonhydrostatic buoyancy residue and the horizontal circulations triggered by the associated pressure gradients. These mechanisms produce significant positive, countergradient momentum flux that counteracts the negative flux production through shear-driven turbulent diffusion near cloud tops. In the smaller 25×25 km^2 BOMEX simulations of Larson et al. (2019) the buoyancy production term and turbulent advection terms are important.

Following these recent studies, the simulations we carry out here to study momentum transport have realistically varying large-scale forcings and use a domain much larger than that of previous LES studies. Our study focuses on the first 9 days of February 2020 during the EUREC^{4}A campaign (Stevens et al. 2021), that we simulated with the Dutch Atmospheric Large Eddy Simulations (DALES; Heus et al. 2010) on a 150×150 km^2 domain forced with large-scale dynamical tendencies from the regional weather model HARMONIE–AROME (Bengtsson et al. 2017; de Rooy et al. 2022).

The EUREC^{4}A campaign provided observational estimates of large-scale wind and pressure gradients as well as large-scale divergence (subsidence) through circular dropsonde arrays—a dataset named JOANNE (George et al. 2021b). Nuijens et al. (2022) used the JOANNE dataset to derive the momentum budget of the trades and showed that into February, as the trade winds strengthened and the cloud field organized into gravel and flower structures, the effect of different flows on the wind may change substantially. For instance, as the winds strengthened, the derived observed amount of vertical divergence of momentum flux appeared to accelerate winds in the upper cloud layer. The in situ turbulent momentum fluxes measured by different aircraft vehicles also suggested that horizontal gradients of momentum flux can be large across 20-km flight legs, suggesting that horizontal homogeneity is a poor assumption, and horizontal flux divergence may not be neglected.

Our objectives are threefold: 1) reveal which scales are contributing to momentum fluxes throughout the boundary layer, 2) study changes in the scale contribution as the cloud field organizes, and 3) study the impact of different scales of momentum transport on the vertical flux divergence. With that, the simulations may provide insight into what the observed momentum budget during EUREC^{4}A appears to suggest: that in organized shallow convection, just as in deep convection, (sub)mesoscale flows $\mathcal{O}(2–100)$ km play a nonnegligible role in the momentum budget.

The paper is structured as follows: Section 2 introduces the experimental design (sections 2a–2d), and it explains a filtering method that is used to partition the flux into different contributing scales (section 2e). The results first describe the simulated wind and cloud field, along with the momentum fluxes (section 3). Section 4 shows the temporal evolution of the momentum flux (section 4a), the spatial scales that contribute to the flux (sections 4b and 4c), and how this varies with precipitation and degree of organization (section 4d). In section 5 we explain the influence of mesoscale flows in (un)organized cloud fields. The discussion and conclusions are given in section 6.

2. Experimental design

a. EUREC^{4}A

The EUREC^{4}A field campaign took place in the oceanic trade winds region east of Barbados, between January and February 2020. EUREC^{4}A is among the largest observational field campaigns of the coupled atmosphere–ocean system, providing benchmark measurements for a new generation of models and scientific discoveries. EUREC^{4}A aims at advancing understanding of the interplay between trade wind clouds, convection and circulation and their role in climate change. EUREC^{4}A also includes a modeling component that consists of a model intercomparison (MIP) case for LES and storm-resolving models (SRMs). Among the goals of this intercomparison are 1) assessing the simulation capability of the observed shallow cloud mesoscale organization over the subtropical ocean, and 2) understanding the underlying dynamical processes leading to the mesoscale organizational patterns. The simulations presented in this study run from 2 to 10 February 2020, which are interesting days because of the range of cloud patterns observed during a transition from weaker to stronger

trade winds. These simulations have largely been used to establish the framework and the set up of the EUREC⁴A-MIP. While the intercomparison case uses large-scale forcing derived from ERA5, this study derives its forcing from the regional weather model HARMONIE–AROME. The latter allows a comparison between the parameterized physical tendencies from the regional model with the resolved physical tendencies of the LES, as described below.

b. HARMONIE–AROME

In this paper we use version cy43 of the numerical weather prediction model HARMONIE–AROME. A general overview of HARMONIE–AROME cy40 can be found in Bengtsson et al. (2017). Most modifications in the physics from model version cy40 to cy43, as well as a comprehensive description of the most relevant parameterizations, namely, the cloud, turbulence, and convection scheme, are presented in de Rooy et al. (2022). The total turbulent fluxes are parameterized using the EDMF framework which facilitates a unified description of the turbulent transport in the dry convective boundary layer (Siebesma et al. 2007) and the cloud-topped boundary layer (Soares et al. 2004; Rio and Hourdin 2008). In such an approach the total turbulent transport is described by a small-scale, diffusive part and a larger-scale transport by organized updrafts.

Diffusive, smaller-scale turbulent transport is described by the TKE turbulence scheme HARMONIE with RACMO Turbulence (HARATU) as described in Lenderink and Holtslag (2004). The shallow convection scheme, as described by de Rooy et al. (2022), utilizes a mass-flux approach in which dry and moist updrafts are distinguished (Neggers 2009). The variables treated in the shallow convective scheme are temperature, humidity, and momentum. This means that the CMT is simply the mass flux times the excess of the updraft u or v. The only difference with scalar variables concerns the initialization of the updraft properties at the lowest model level. Temperature and humidity have an initial excess over the environmental values scaled by the surface fluxes, whereas u and v have the same values for the updraft and the environment. As the updraft rises, the environment changes and entrainment dilutes the updraft, together determining the excess of the updraft in both scalars and momentum at higher levels.

HARMONIE–AROME (from hereon HARMONIE) is used with a grid spacing of 2.5 km in an area of 3200×2025 km² centered around Barbados. HARMONIE runs in a free (climate) mode starting on 1 January and is forced with ERA5. In climate mode, HARMONIE is not reinitialized every 24 h, which limits the effect of biases inherited from the forcing model. However, HARMONIE receives lateral boundary fields from ERA5 every hour. With this setup the model is allowed to develop its own synoptic systems which we assume to be plausible although we recognize they are different from the real, observed meteorological conditions.

c. DALES

As described in Heus et al. (2010), DALES is a community-based model and it is freely available. In this study we use DALES version 4.3. Under anelastic approximation, the model solves filtered prognostic equations in finite volumes. The model uses doubly periodic boundary conditions on the domain sides, no-slip condition at the bottom and a sponge layer at the top. Advection is done using a fifth-order central difference scheme (Wicker and Skamarock 2002). Subfilter-scale fluxes are modeled through an eddy diffusivity approach, following Deardorff (1980). Monin–Obukhov similarity theory is applied for the computation of the surface fluxes for heat, moisture, and momentum at the bottom boundary of the model. For condensation a traditional adjustment scheme is used, and a two-moment scheme (Khairoutdinov and Kogan 2000) is used for rain, while in the cloud microphysics a constant cloud droplet number concentration of 50 cm⁻³ is prescribed.

The EUREC⁴A simulations are run on a domain of 150×150 km², centered at 13.3°N, −57.7°E, which covers an area of intensive measurements eastward of Barbados. In both x and y directions, 1512 horizontal grid points are used, which corresponds to a grid spacing of about 100 m. The vertical grid is stretched with the following exponential function: $dz_i = 20(1 + 0.012)^i$, where dz is the grid spacing, and i is the level. This gives a dz of 20 m near the surface and about 55 m at 3 km. The domain extends up to 8 km, with a sponge layer occupying the upper one-third of its levels. Above this simulated domain lies a horizontally homogeneous layer with prescribed profiles of pressure, temperature, humidity, and ozone. These so-called background profiles serve as inputs for a rapid radiation transfer model. DALES is run in a climate mode without reinitialization, whereby the first four hours are disregarded as spinup. This mode allows aggregated cloud fields and mesoscale circulations to evolve over multiple days.

d. Large-scale forcing

The regional weather model HARMONIE provides the initial conditions, sea surface temperature (SST), and large-scale dynamical forcing (tendencies) of momentum, temperature, and humidity to DALES. At the surface the SST is prescribed daily, and the roughness length is kept constant at 10^{-5} m. This means that our results exclude the effect of a diurnality in SST (not captured by HARMONIE).

Throughout the layers, the large-scale forcing is applied as one dynamical tendency that includes both vertical and horizontal advective tendencies as well as the large-scale pressure gradient and Coriolis force (for momentum). The tendency equation (here for the zonal wind u) can be split into two parts as follows:

$$\frac{\partial \overline{u}}{\partial t} = \left(\frac{\partial \overline{u}}{\partial t}\right)_{\text{forcing}} + \left(\frac{\partial \overline{u}}{\partial t}\right)_{\text{DALES}}, \quad (1)$$

where the overbar defines the spatial average over a horizontal slab of the DALES domain. The two terms on the rhs represent, respectively, 1) the large-scale forcing from HARMONIE, and 2) the tendencies calculated by DALES for scales smaller than the computational domain. The large-scale forcing includes

$$\left(\frac{\partial \overline{u}}{\partial t}\right)_{\text{forcing}} = -\overline{\mathbf{v}} \cdot \nabla \overline{u} + \frac{\partial \overline{p}}{\rho \partial x} + f\overline{v} + \mathcal{F}_{\text{nudge}}, \quad (2)$$

where ρ is the reference density, $\mathbf{v} = (u, v, w)$ is the wind vector, $\overline{\mathbf{v}} \cdot \nabla \overline{u}$ represents the horizontal and vertical advection of

momentum, $\partial \overline{p}/\rho \partial x$ is the pressure gradient term, $f\overline{v}$ is the Coriolis force, and $\mathcal{F}_{\mathrm{nudge}}$ is the tendency introduced by the nudging to the HARMONIE profiles. All terms in Eq. (2) are calculated hourly on a 300×300 km^2 subdomain of HARMONIE, which encompasses the DALES domain. These forcing and profiles are then spatially averaged and imposed uniformly to DALES. The relatively weak nudging is applied separately on an hourly basis with a time scale that changes with height: above 3 km it is 6 h, at 2.5 km it is 28 h, and it becomes increasingly negligible at lower levels.

The second term on the rhs of Eq. (1) is the turbulent momentum flux divergence term as calculated by DALES:

$$\left(\frac{\partial \overline{u}}{\partial t}\right)_{\mathrm{DALES}} = -\frac{1}{\rho}\frac{\partial}{\partial z}\rho\overline{u'w'}. \qquad (3)$$

The horizontal flux divergence is omitted because of the periodic boundary conditions. In section 5 we make use of the Boussinesq approximation to drop density dependencies and rewrite Eq. (3) as

$$\left(\frac{\partial \overline{u}}{\partial t}\right)_{\mathrm{DALES}} = -\frac{\partial}{\partial z}\overline{u'w'}. \qquad (4)$$

e. Subfilter and up-filter partitioning of turbulent fluxes

To evaluate the contribution of different scales to momentum transport, we apply Reynolds decomposition and obtain momentum fluctuations with respect to the horizontal domain average on 3D fields that are low-pass filtered with different filter sizes. This effectively partitions the total flux into a subgrid and a resolved component (see also Honnert et al. 2011; Dorrestijn et al. 2013).

The low-pass spectral filter uses a two dimensional Fourier transform and a cutoff frequency in Fourier space [see appendix 1 in Honnert (2019) for other procedures], and returns all fluctuations occurring at the subfilter scales. Small filter sizes correspond to high wavenumbers. The smallest possible filter has the size of a grid box and returns no fluctuations, indicating that all variance is carried at scales larger than the specific size (up-filter). [To obtain Figs. 6 and 9, the partitioning is done repetitively at 40 different filter sizes, from 100 m to 150 km, to uniformly cover the range of scales in the domain (or spectrum of wavenumbers in the Fourier space).] The partitioning can be described with the following set of equations:

$$\begin{aligned} u' &= u'_{\mathrm{SF}} + u'_{\mathrm{UF}}, \\ w' &= w'_{\mathrm{SF}} + w'_{\mathrm{UF}}, \end{aligned} \qquad (5)$$

where u' and w' indicate the fluctuations with respect to the horizontal slab average, and the subscripts SF and UF refer to the sub- and up-filter scales, respectively. The turbulent momentum flux averaged over the DALES domain can be written as

$$\begin{aligned} \overline{u'w'} &= \overline{(u'_{\mathrm{SF}} + u'_{\mathrm{UF}})(w'_{\mathrm{SF}} + w'_{\mathrm{UF}})} \\ &= \overline{u'_{\mathrm{SF}}w'_{\mathrm{SF}}} + \overline{u'_{\mathrm{UF}}w'_{\mathrm{UF}}} + \overline{u'_{\mathrm{SF}}w'_{\mathrm{UF}}} + \overline{u'_{\mathrm{UF}}w'_{\mathrm{SF}}}, \end{aligned} \qquad (6)$$

which simplifies to

$$\overline{u'w'} = \overline{u'_{\mathrm{SF}}w'_{\mathrm{SF}}} + \overline{u'_{\mathrm{UF}}w'_{\mathrm{UF}}}, \qquad (7)$$

because high- and low-pass filtered functions with the same cutoff wavenumber are orthogonal (Frisch 1995). In Eq. (7) the first term on the rhs is the flux carried at scales smaller than the size of the filter, the second term is the flux carried at scales larger than the size of the filter.

Within the 150×150 km^2 DALES domain submesoscale and mesoscale flows are present and in this study, we consider the contribution of all of these to what would be a Reynolds averaged flux over an area representative of the current resolution of global climate models (50–100 km). Current generation weather models are often in the so-called gray zone of convection as they use a grid mesh far less than $\sim$50 km and thus explicitly resolve some mesoscale flows. The contribution of scales and a discussion on which flux needs to be parameterized will follow in sections 4 and 6.

3. Simulated and observed atmospheric conditions

The 9 days of EUREC^{4}A simulations between 2 and 10 February were characterized by a significant evolution in winds and cloud patterns. It was chosen specifically to simulate the somewhat deeper and more vigorous trade wind convection that develop as winds strengthen. Figure 1a shows a time series of the domain-averaged cloud fraction in DALES, along with the temporal evolution of the rain rate (solid red line in Fig. 1a), and the surface zonal and meridional wind (Figs. 1b,c) from DALES, HARMONIE, ERA5 and from the HALO dropsondes and R/V *Meteor* radiosondes. Along with the time series, the simulated liquid water path (LWP) in Fig. 2 shows the model's ability to reproduce different cloud patterns on different days, which have been identified from GOES satellite imagery as *flowers* on 2 February, *sugar* on 6 February, and *gravel* on 7 and 9 February (Schulz 2022). The full evolution of the simulated cloud pattern is available as online supplemental material.

The black line in Fig. 1a indicates the cloud-top height, which is defined as the level where the averaged liquid specific humidity becomes negligible ($ql < 0.0001$ g kg^{-1}), above the level where ql maximizes. Precipitating shallow clouds reach up to 2.5 or 3 km on most days. Despite being over ocean, the cloud top oscillates significantly, ranging from about 1 km to almost 4 km. The variability reflects the diurnality, with deepening cloud trends during the morning hours, and a general deepening of the cloud layer over the 9 days as surface wind speeds increased.

On 2 February, after 0800 LT, a persistent thin layer of clouds between 2 and 2.5 km appears, which is typical of the stratiform anvil associated with flowers. The flower patterns and associated cold pools are still present on 3 February, as seen in the LWP field in Fig. 2a. The anvil can persist, as in this case, after the convective area of the cloud has dissipated by rain. On 6 February, the cloud fraction is relatively low, but constant throughout the day and with a maximum near cloud base and a cloud top near 2 km. On this day, DALES shows unorganized sugar clouds (see Fig. 2b) with almost zero
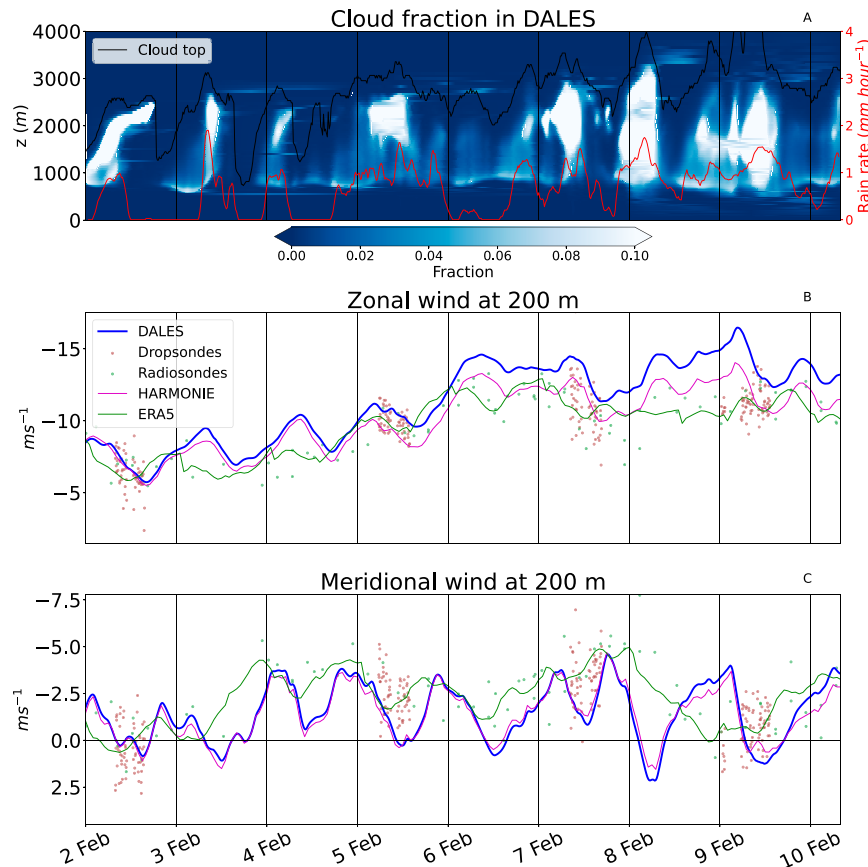
FIG. 1. Time series of simulated quantities, where every vertical black line is at 0000 LT. (a) The mean cloud fraction and precipitation rate from DALES. The (b) zonal and (c) meridional wind at 200 m, where we also included HARMONIE (magenta), ERA5 (green), and observations (dots).

rain rate (red line) at the surface. This is in line with the observations. Gravel patterns are also clearly reproduced in our simulation on 8 and 9 February (see Fig. 2c). On these days, the cloud layer deepens and large cold pools develop, but the cloud patterns are less regular or symmetric as in the flower case of Fig. 2a.

The diurnality in the clouds and precipitation is evident, with the deepest and rainiest clouds around 0700 local time
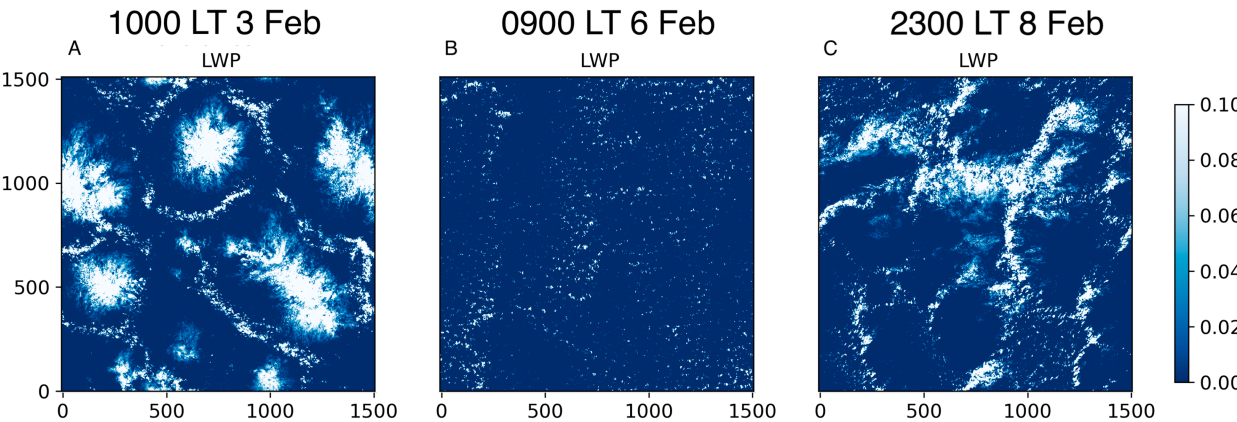

FIG. 2. Examples of simulated fields of liquid water path (LWP). The time corresponds to (a) 1000 LT 3 Feb, (b) 0900 LT 6 Feb, and (c) 2300 LT 8 Feb.
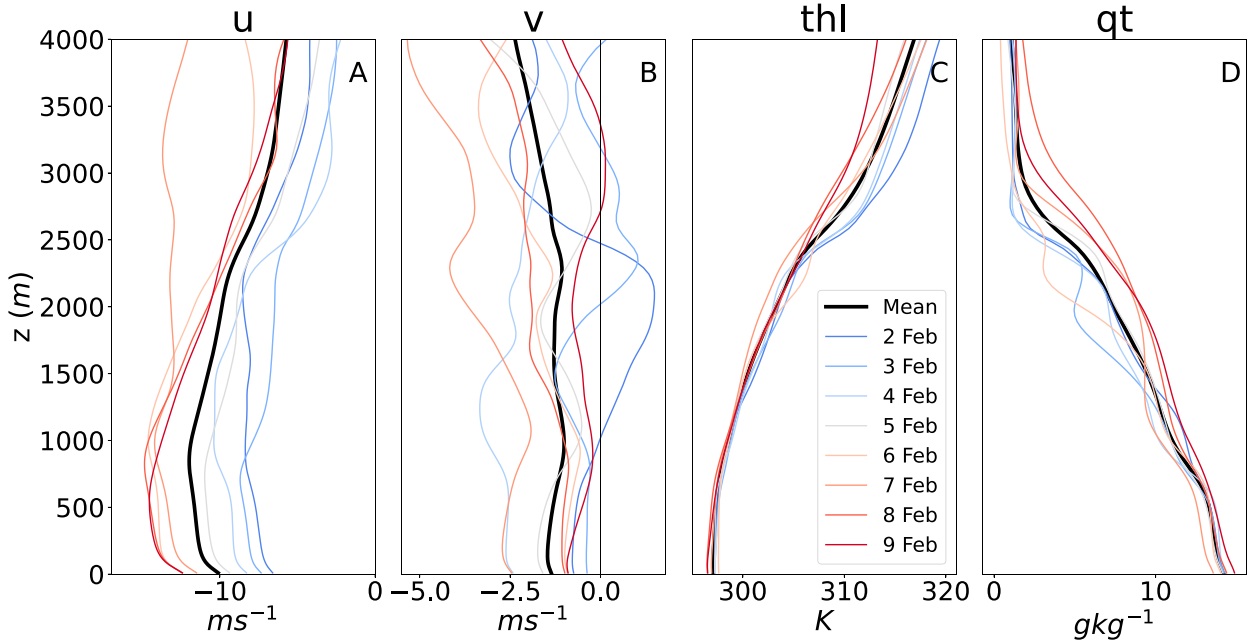
FIG. 3. Domain-averaged profiles. Black is the mean over the entire dataset, and each colored line refers to a single day. (a) The zonal wind, (b) the meridional wind, (c) the liquid potential temperature (thl), and (d) the total specific humidity (qt).

(LT). A diurnality in cloudiness and wind is supported by observations, although less strong than in HARMONIE and DALES. Vial et al. (2019, 2021) found two populations of cumuli with different diurnality: 1) nonprecipitating very shallow cumuli that develop during the day and maximize around sunset and 2) deeper precipitating cumuli with stratiform cloud layers below the trade inversion that develop during the night and maximize before sunrise. The deeper ones dominate the diurnality of the total cloud cover.

The diurnality in surface winds has been argued as one of the possible drivers of the diurnality in clouds, besides differences in radiative heating rates between day and night. Strongest winds occur at 0600 LT, shortly before the peak in precipitation and cloud cover. The simulated winds evolve in a similar way as the radiosonde and dropsonde winds, but biases increase in the last 4 days, which is not unexpected given that the simulations are not reinitialized at midnight. During the final days, the surface sensible heat flux (not shown) is also larger in DALES than observed. Differences with ERA5 and the observations are expected in such climate runs. The excessive diurnal cycle, which DALES inherits from HARMONIE, is a known problem and it should be discussed in a separate article, as diurnality is not the focus of this study. From Fig. 1 emerges that DALES and HARMONIE are in good agreement with each other. After 6 February the strong large-scale forcing in the zonal component challenge the double periodic boundary conditions resulting in winds that are stronger in DALES than in HARMONIE. We assume that these somewhat stronger winds are still probable in the trade region.

Daily mean profiles of the simulated winds and thermodynamic structure are shown in Fig. 3. The days with strong zonal winds near the surface (the second half of the simulated days, 6–10 February, in orange/red in Figs. 3a,b) tend to have larger shear in the cloud layer, except for 7 February, which exhibits a deep layer of strong easterlies. The meridional winds are more variable but overall negative (northerly winds). On the first few days (blue) the inversion is well pronounced around 2500 m, and capped by a relatively warm and dry free troposphere. In contrast, on the last few days (red lines) the inversion is less evident and the profiles indicate heat and moisture mixing across a deeper layer, in line with the presence of deeper and more vigorous convection.

4. Characteristics of the momentum flux

a. Mean momentum flux profiles

The daily-mean total (resolved plus unresolved) zonal momentum flux profiles in DALES (Fig. 4a) are typically positive near the surface and turn negative between 1 and 1.5 km (above cloud base). A positive momentum flux up to 1 km is consistent with local turbulence: for an easterly flow ($\overline{u} < 0$), upward ($w' > 0$) motions generate positive zonal wind anomalies ($u' > 0$), while downward motions ($w' < 0$) generate negative zonal wind anomalies ($u' < 0$). As the evolution of the flux in Fig. 4b shows, the near-surface zonal momentum flux almost doubles in the last 4 days, in line with the strengthening of the easterly surface wind, and the height at which the flux turns negative increases. Large values of momentum above 2 km are found more frequently
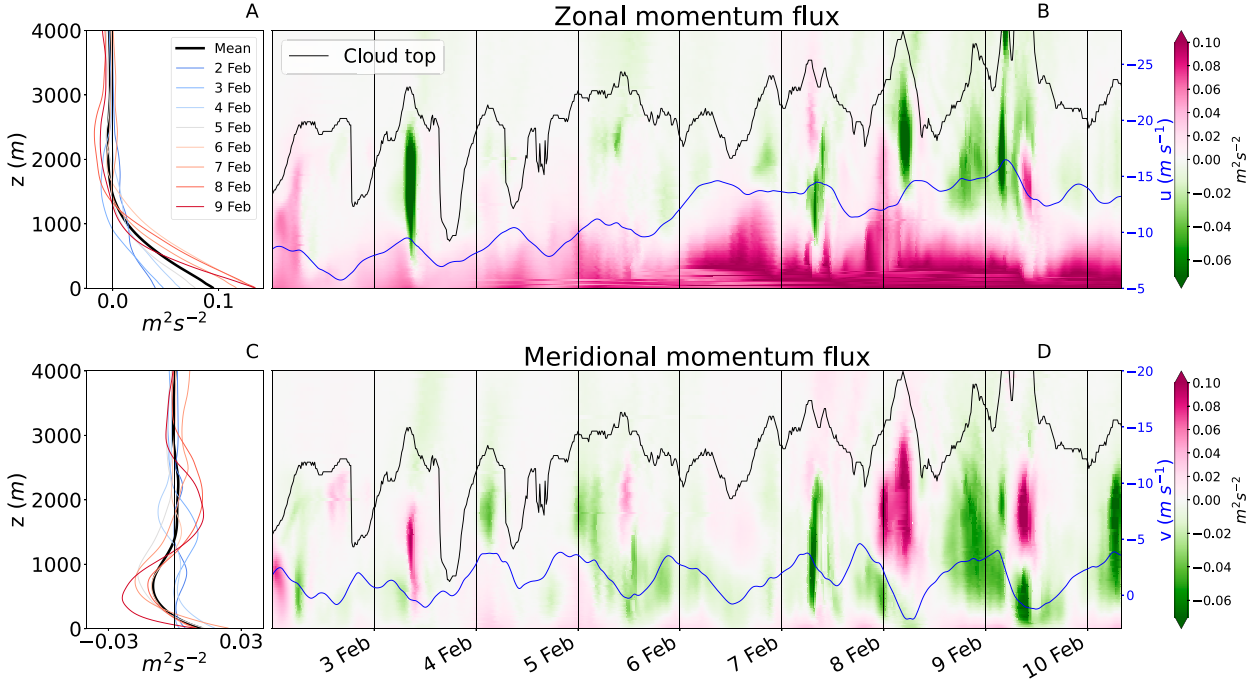
FIG. 4. (a),(b) Zonal and (c),(d) meridional momentum flux profiles, shown (a),(c) as daily averages and (b),(d) as contours of 15-min averages. The black line in (b) and (d) marks the cloud-top height (h_b), while the blue lines indicate the surface zonal and meridional momentum.

during the final days of simulation and correspond to increases in cloud-top height (shown as a black line).

As seen in Fig. 3a, the zonal wind shear becomes positive around 1 km ($du/dz > 0$), whereas the zonal momentum flux remains positive up until ~1.3 km ($\overline{u'w'} > 0$). This implies a layer where, in a simple K-diffusion model, the turbulent diffusivity parameter K is negative, denoting countergradient momentum transport.

The meridional momentum flux (Figs. 4c,d) is smaller compared to the zonal momentum flux. It is positive at the surface and negative between 200 and 1200 m on most days. The sign of the meridional momentum flux is less trivial to interpret because, at times, the meridional wind can turn southerly (positive), as seen in Fig. 1c. Negative fluxes near the surface are associated with hours of southerly winds, typically occurring during daytime. The largest values of meridional momentum flux are inside the cloud layer on days with stronger convection (last 4 days).

In Figs. 4b and 4d convective events range from few hours (e.g., 3 February) to more than 5 h (e.g., 8 February) and go hand in hand with strong momentum fluxes in the cloud layer. These strong variations are not always evident from the daily-mean profiles. Even more pronounced is the spatial heterogeneity in the momentum flux across the domain, which we present next.

b. Spatial heterogeneity

Figure 5 shows a snapshot of the momentum flux at 200 m at 1000 LT 3 February (the flower case of Fig. 2a). Figures 5a and 5b show, respectively, the total zonal and meridional flux.

The subfilter flux (for a filter $\Delta x = 2.5$ km) is in Figs. 5c and 5d, whereas the up-filter flux is in Figs. 5e and 5f.

The total (resolved plus subgrid) zonal flux is 0.037 m² s⁻², of which 65% (0.024 m² s⁻²) is carried by scales smaller than 2.5 km and 35% (0.013 m² s⁻²) by larger scales, even near the top of the surface layer. The total meridional flux $\overline{v'w'}$ is 0.0178 m² s⁻², of which 52% is carried by scales smaller than 2.5 km ($\overline{v'_{SF}w'_{SF}} = 0.0092$ m² s⁻²), and 48% by scales larger than 2.5 km ($\overline{v'_{UF}w'_{UF}} = 0.0086$ m² s⁻²). Because of the large spatial heterogeneity in the sign of the flux, domain-averaged fluxes suggest a much smaller momentum flux than there is on a more local scale.

Below the flowers, Fig. 5 captures several large cold pools, which appear as circles of diverging wind with a diameter of about 50 km. The combination of positive and negative signs in the horizontal wind anomalies divides the cold pool into four parts. Upwind, the momentum flux is positive at the edge and negative between the edge and the center of the structure; downwind, the momentum flux is negative at the edge, and positive between the edge and the center. These mesoscale structures are clear in the up-filter flux fields of Figs. 5e and 5f and are partly visible also at the subfilter scales (Figs. 5c,d). To generalize beyond this one scene, the next section analyzes the scales responsible for momentum transport using all available statistics. The up-filter momentum flux for all scenes is available in the online supplemental material.

c. Scales of momentum transport

The relative contribution of different scales to the total momentum flux is shown in Fig. 6. This essentially shows the
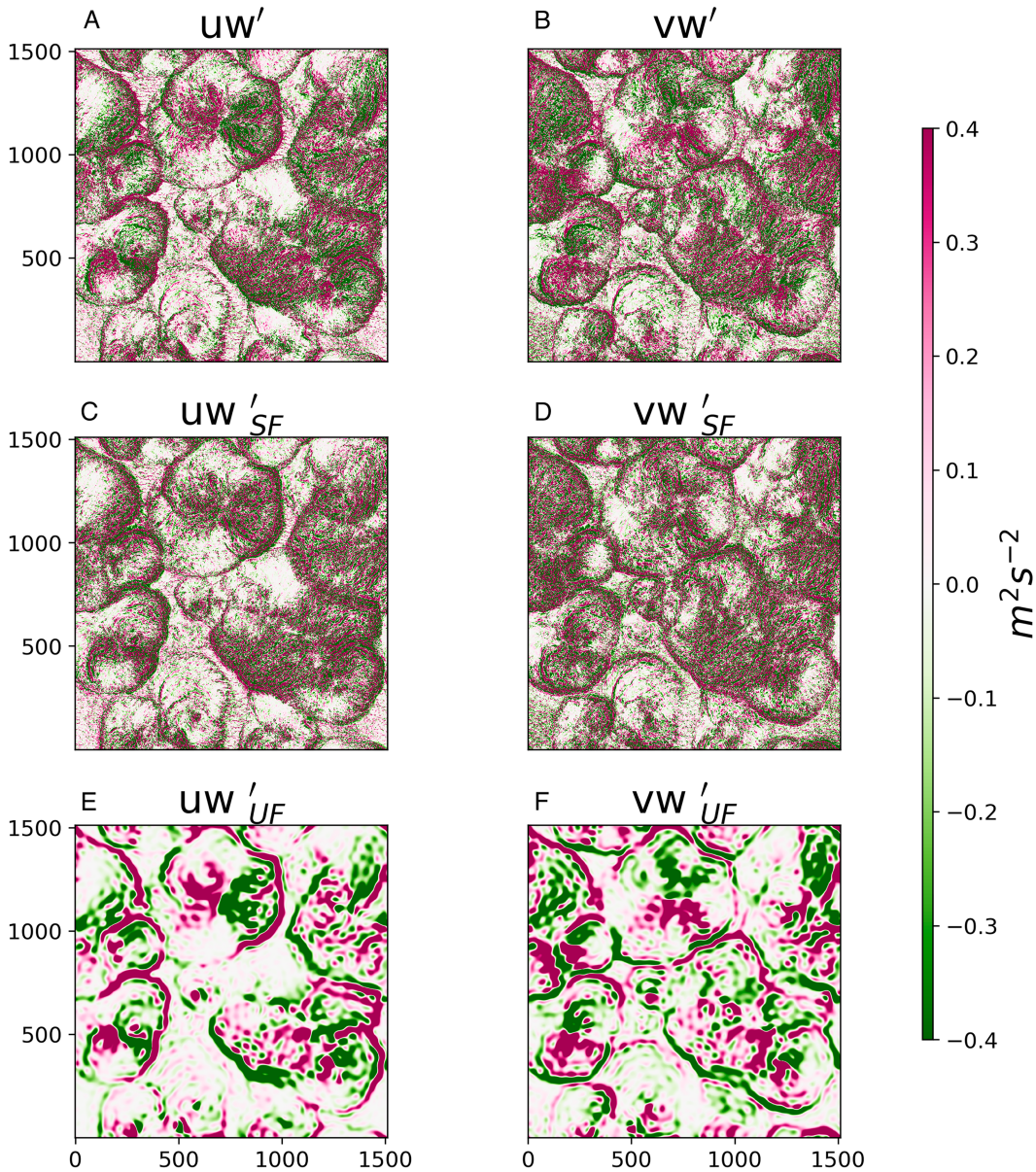
FIG. 5. Instantaneous fields at 200 m at 1000 LT 3 Feb for resolved (left) zonal and (right) meridional momentum fluxes from DALES. (a),(b) The total resolved flux: $\overline{u'w'} = 0.037$ m^2 s^{-2}, $\overline{v'w'} = 0.018$ m^2 s^{-2}. (c),(d) The subfilter resolved flux for $\Delta x = 2.5$ km: $\overline{u'_{SF}w'_{SF}} = 0.024$ m^2 s^{-2}, $\overline{v'_{SF}w'_{SF}} = 0.01$ m^2 s^{-2}. (e),(f) The up-filter resolved flux: $\overline{u'_{UF}w'_{UF}} = 0.013$ m^2 s^{-2}, $\overline{v'_{UF}w'_{UF}} = 0.009$ m^2 s^{-2}.

change of the subfilter component as a function of increasing filter size, here for the momentum fluxes simulated in the middle of the cloud layer, as it displays the largest variability. The y axis is normalized by the total flux in the domain. Figures 6a and 6b show the zonal momentum flux ($\overline{u'_{SF}w'_{SF}}$) and Figs. 6c and 6d show the meridional momentum flux ($\overline{v'_{SF}w'_{SF}}$). Following Honnert et al. (2011) in Figs. 6a and 6c a dimensionless x axis is created by scaling the size of the filter with the height of the subcloud plus cloud layer (h_b). The vertical black line

marks the mesh at which the filter size Δx equals h_b. This height varies in time, which explains why the lines begin and end at different points on the x axis. In Figs. 6b and 6d the flux partition is plotted against the size of the filter only and the vertical line marks $\Delta x = 2$ km. Hereafter we refer to the mesoscale as all scales between 2 and 150 km, thus the meso-gamma and part of the mesobeta scales. As the dimensionless mesh size and the filter size increase, the contribution of the subfilter scale also increases. Ultimately, 100% of the flux is
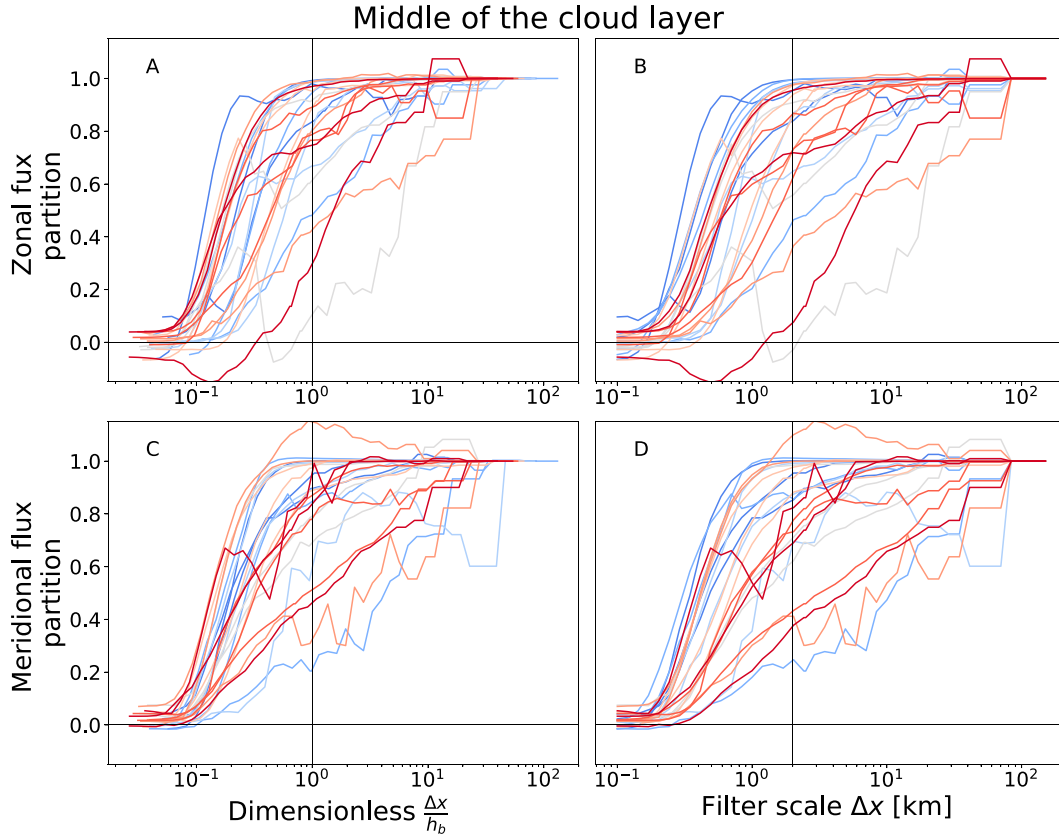
FIG. 6. Partition of the subfilter (a),(b) zonal and (c),(d) meridional momentum flux as a function of (a),(c) the dimensionless mesh $\Delta x/h_b$ and (b),(d) the dimensional filter size Δx. All panels refer to a horizontal cross section in the middle of the cloud layer. The vertical black lines denotes $\Delta x/h_b = 1$ and $\Delta x = 2$ km. Each curve is the median of an 8-h interval identified by the colors: from blue at the beginning of the simulation to red at the end of the simulation.

carried by the subfilter scale when the filter is as large as the domain. The y-axis value at the smallest filter size represents the percentage of the total flux carried by the unresolved scales ($\Delta x < 100$ m). Each curve refers to the median for an 8-h interval and the colors refer to the different days, as in Fig. 3.

The observed spread in scale contribution in the cloud layer is large: at $\Delta x = 2$ km, the subfilter momentum flux (Figs. 6b,d) varies from less than 20% to almost 100% of the total flux. In both directions, scales can contribute negatively to the total momentum flux, making the curves in Fig. 6 nonmonotonic, in line with Zhu (2015). This is because thermally driven plumes or cells do not necessarily possess similar horizontal momentum, whereas they often have similar thermodynamic properties. Furthermore, mesoscale flows associated with organized shallow convection and heating contrasts on even larger scales are introduced. The mesoscales contribute more to $\overline{v'w'}$ than to $\overline{u'w'}$, suggesting that circulations induced by coherent convective structures are more important for transporting meridional momentum than zonal momentum. This is even more evident at lower heights in the boundary layer (as we will see in the next section).

In contrast to Honnert et al. (2011), after rescaling with the cloud-top height, the individual lines do not collapse onto a single curve, which would universally describe the partitioning of the momentum flux as a function of a well-defined vertical scale. Whereas the method proposed by Honnert et al. (2011) might work for thermodynamic variables in a clear boundary layer or for simple nonprecipitating cases, it fails to capture the momentum flux partitioning in organized, precipitating shallow cumulus convection. Cloud-top height, or alternatively the boundary layer height, only captures the vertical growth of a convective system, but is clearly not always correlated with the dominant horizontal length scales, which play an important role in organized cloud fields (Janssens et al. 2021).

The contribution of mesoscales to the momentum fluxes depends strongly on the specific day considered. Figure 7 shows the temporal evolution of the contribution of the subfilter component at $\Delta x = 2$ km. The data are grouped into 8-h intervals, where each interval includes 16 cross sections of flux, whose spread is shown as a boxplot. The median, corresponding to the value at the vertical black line in Figs. 6b and 6d, is indicated with a red line. While on some days for the zonal component (Fig. 7a), the majority of the data suggests a
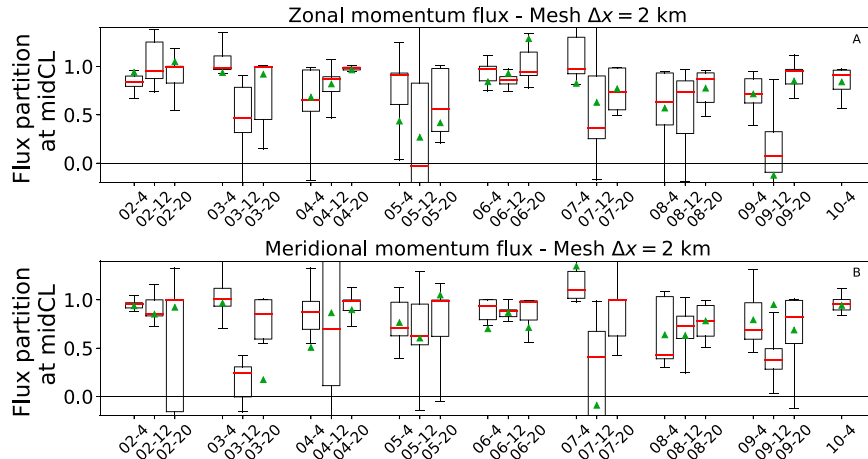
FIG. 7. Distribution of the subfilter (a) zonal and (b) meridional momentum flux in the middle of the cloud layer for a filter $\Delta x = 2$ km. Each boxplot refers to an 8-h interval, thus includes 16 values. The x labels tell the day and central hour of the interval (e.g., 02-04 is 0400 LT 2 Feb), and the green triangles indicate the mean.

contribution of the subfilter scales between 60% and 90%, with relatively small spread, other days suggest a significant increase in the contribution of mesoscales, shown as a reduction of the subfilter contribution. For instance, on 3 February, the winds are slow and large coherent convective structures develop into flowers that dissipate again after a few hours. The smallest variability is on 6 February, where the scales smaller than 2 km consistently carry around 90% of the total flux: $u'_{SF}w'_{SF}/u'w'$ and $v'_{SF}w'_{SF}/v'w' \approx 0.9$. On this day the winds are strong, and only small thermals form, resulting in a persistent sugar-type field (see Fig. 2b). Next, we investigate whether convective organization can explain the shape of the curves in Fig. 6.

d. Influence of precipitation and organization

Spatial organization is quantified using the widely used metric I_{org} applied to fields of LWP (Weger et al. 1992); I_{org} ranges between 0 and 1. A value of 0.5 indicates that objects (clouds) are randomly distributed in space, higher values indicate a clustered and organized field, whereas lower values indicate a regularly distributed field. Using an LWP mask means that anvils and nonconvecting clouds are seen as cloudy objects, possibly overestimating the degree to which dynamically active clouds map onto the momentum fluxes. The different colors in Fig. 8a represent three groups of I_{org}: group 1 (yellow) corresponds to the lower quartile of I_{org} values, group 3 (green) is the upper quartile, and group 2
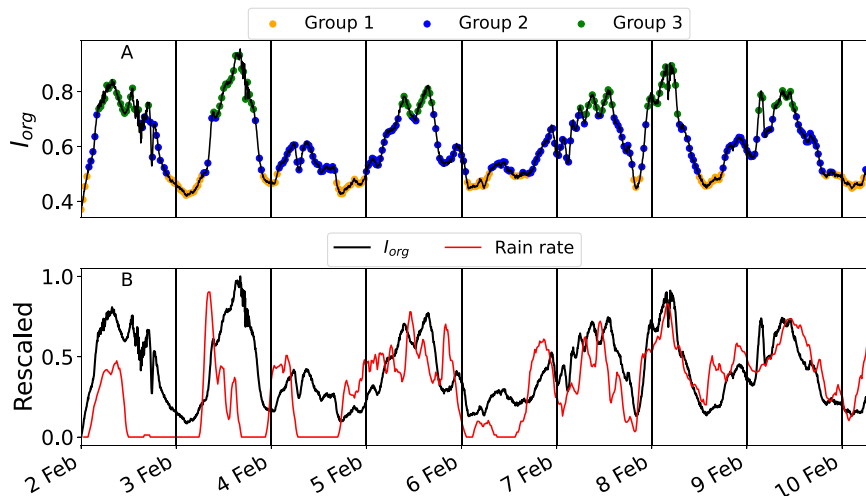

FIG. 8. (a) Time series of I_{org} as a 1.5-h rolling average. Values in the lower quartile are in yellow (group 1), values in the upper quartile are in green (group 3), the remaining values are in blue (group 2). (b) I_{org} (black) and surface rain rate (red) as a 1.5-h rolling average and rescaled between 0 and 1.
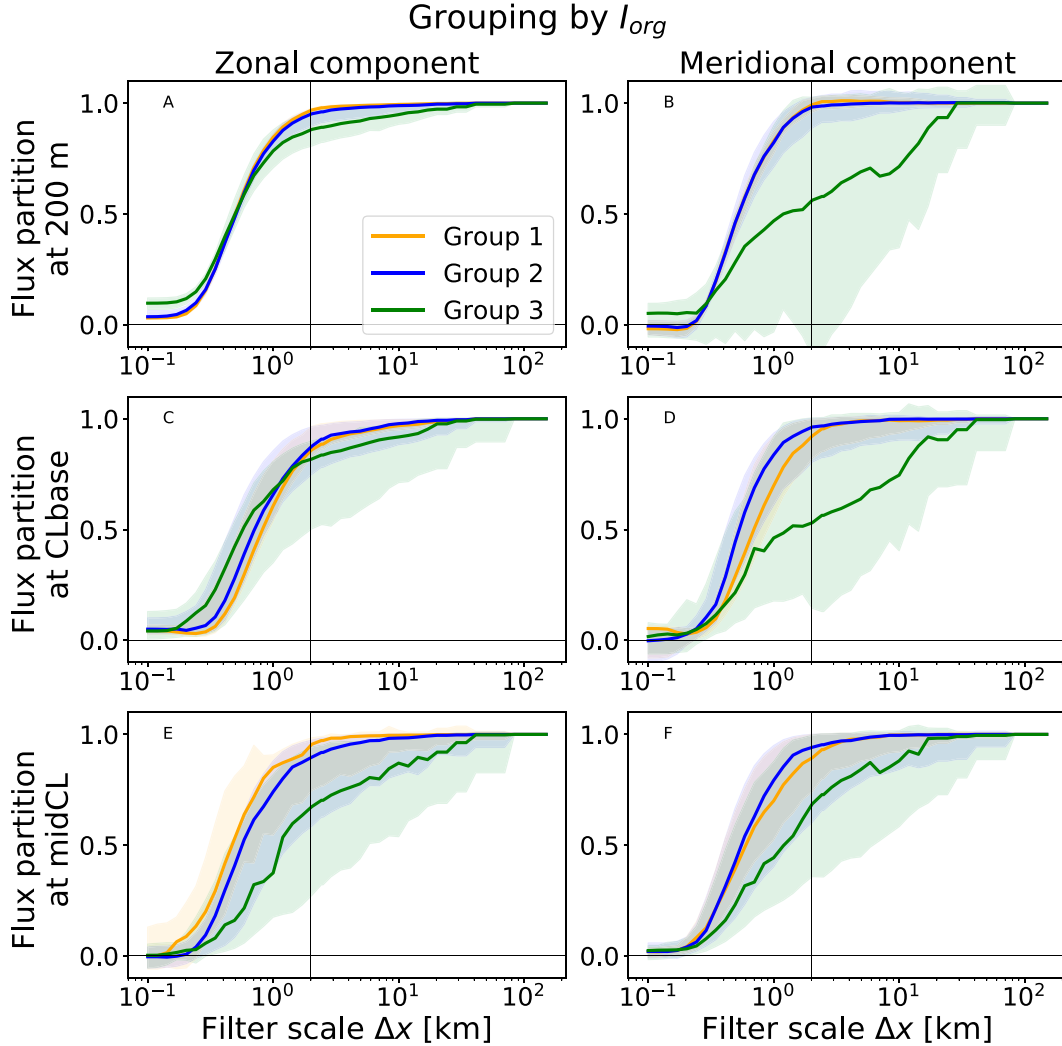
Grouping by I_{org}

FIG. 9. Partition of the subfilter momentum flux as a function of the filter size Δx. The vertical black line denotes $\Delta x = 2.5$ km, and each row refers to a different height: (a),(b) 200 m, (c),(d) cloud base, and (e),(f) the middle of the cloud layer. Each color refers to one of the groups based on I_{org}. Group 1 is in yellow, group 2 is in blue, and group 3 is in green. See the text for a description of the groups.

(blue) includes the remainder. The analysis gives similar results when creating groups defined by rain rate, but in line with Radtke et al. (2022), the two indices have some differences: I_{org} can be high on the first 2 days although precipitation (and total momentum fluxes in Fig. 4) is moderate.

Precipitation is shown to precede organization on the first few days of the simulation, which may be typical of flower structures, where anvils persist long after rain events have killed the source of convection. Differently, with gravel and mixed cloud structures (e.g., on 8 February) precipitation and organization tend to have local peaks at the same time. Figure 8 is also informative concerning the observed diurnal cycle of shallow convection in the trades (Vial et al. 2019; Radtke et al. 2022). The early morning typically brings more vigorous convection, which is reflected as peaks of rain rate and I_{org} around

1000 LT. Lowest rain rates are in the evening, and unorganized fields typically occur around 0000 LT.

Hereafter we analyze the flux partitioning as a function of scale for the three groups identified with I_{org}. Figure 9 shows results for three heights: 200 m (Figs. 9a,b), at cloud base (Figs. 9c,d), and in the middle of the cloud layer (Figs. 9e,f), as was shown before. Group 1 (yellow lines) tends to capture scenes where the small scales are the most active and the sub-filter scales dominate over 90% of the total flux for $\Delta x = 2$ at all levels. In group 3 (green lines) on the other hand only 70%–80% of the flux is carried by scales smaller than 2 km in the cloud layer. The different spread (smallest in group 1 and the largest in group 3) is partly explained by the different range of I_{org} values in the two groups. In group 1 I_{org} ranges between 0.37 and 0.5, whereas in group 3 I_{org} ranges between 0.72 and 0.96.

The separation of the data by I_{org} thus helps explain the spread in scale behavior seen in Fig. 6, with more mesoscale contribution to the flux higher up in the boundary layer than near the surface. However, for the meridional momentum flux, the mesoscales already have an imprint near the surface, because the meridional wind and thus meridional wind stresses are comparably small. Instead, for the zonal momentum flux, large small-scale turbulent stresses due to stronger zonal winds at the surface still lead to a dominance of smaller scales.

The scale behavior of the heat and moisture flux is shown in the appendix. Much like the meridional momentum flux, these thermodynamic variables have a large imprint of mesoscales near the surface for groups 2 and 3 (see appendix). In the cloud layer, heat and moisture tend to be carried vertically at smaller scales than momentum, although with small differences, especially in group 2.

5. Role of (organized) convective momentum transport

From section 4 we can infer that, for scales of 1–10 km, there is not a clear, constant separation between scales in carrying momentum transport. In the following, we will use the definition of mesoscales and a filter size of 2 km to study how momentum transport on scales smaller and larger than 2 km influences the momentum budget by means of its vertical flux divergence. This is done for the unorganized and organized groups: sections 5a and 5b, respectively.

a. Momentum flux divergence in unorganized shallow convection

The mean zonal wind shear in the lowest I_{org} group is negative below 1 km and positive above (Fig. 10a), with a pronounced wind jet just above cloud base. Near the surface, the total resolved zonal momentum flux (solid green in Fig. 10b) is larger than the average shown in Fig. 4. The countergradient transport layer (marked in red on the y axis) is small between 1 and 1.5 km.

The (northerly) meridional wind also has a small local maximum at the top of the surface layer and then decreases up to 2.5 km (Fig. 10d). The small local maximum implies a narrow layer of countergradient momentum transport up to 300 m, while everywhere above 300 m, the meridional momentum flux is negative, sustaining downgradient momentum transport in the cloud layer. The up-filter flux (brown line) maximizes around cloud base and its relative contribution is small both in the zonal and meridional direction. In other words, at all heights, scales smaller than 2 km (subfilter) carry the majority of the momentum flux.

The vertical divergence of the momentum flux (Figs. 10c,f) indicates an acceleration where $-(\partial/\partial z)\overline{u'w'} < 0$, because of the negative sign of the zonal wind. Scales smaller than 2 km decelerate the zonal wind at all heights, but least so near cloud base, as shown in Helfer et al. (2020) and Dixit et al. (2021). Meridional winds are decelerated below cloud base, while they accelerate in a layer above cloud base. The up-filter zonal momentum flux (brown line) is symmetric around cloud base and introduces a deceleration. The positive sign of the

up-filter flux can be explained by the tilting of the coherent overturning cells that are responsible for this transport. According to Moncrieff (1992) momentum transport by organized eddies propagating in a shear flow is a fundamental property of their tilt relative to the shear vector. Hence, these coherent cells must be tilted in the direction of the shear vector (du/dz): downshear (to the west) when defined as the zonal wind at cloud top minus the zonal wind at 200 m. In that case, the upward ($w' > 0$) branches of these cells move to the west ($u' > 0$), leading to $u'w' > 0$. With transport maximizing near cloud base, the flow below is experiencing a net acceleration that opposes the friction imposed by turbulence and convection, while in the cloud layer, it contributes to a "cumulus friction." Vertically integrated, the mesoscale momentum flux tendency is zero, which means that mesoscale circulations merely rearrange momentum.

b. Organized convective momentum transport

In group 3 of large I_{org}, up-filter scales carry more than 50% of the momentum flux everywhere above cloud base (Figs. 11b,e). The mean cloud top of this group is a few hundred meters higher than in unorganized cases, but one should consider that convection often extends above this mean value (Fig. 4), as suggested by the negative zonal fluxes above 2 km. As such, the layer with nonzero momentum flux is deeper in this group.

The wind profiles are notably different from the unorganized cases, with weaker winds near the surface and much smaller meridional winds in the subcloud layer. Above 1 km the zonal winds are well mixed with little vertical shear and a deep layer of countergradient transport. The meridional winds are negatively sheared and a thin layer of countergradient transport appears also in the meridional component between 800 m and 1 km.

In the lower cloud layer, the sign of the up-filter zonal momentum flux is positive, which means that the coherent or mesoscale overturning cells are tilted down-shear, but they become tilted up-shear above 2 km, and momentum fluxes there turn negative. Apparently, the mesoscale cold pool structures near the surface do not generate much up-filter momentum flux there when averaged over the domain, which must be because the diverging and converging branches of cold pools are symmetric and of opposite sign (see Fig. 5).

In the meridional direction, the mesoscale flux is negative below 1 km, which implies a strong tilting up-shear despite the near-zero mean shear that is present. The deceleration (positive flux divergence) that is a result of this may help contribute to the profile of meridional wind. In the cloud layer, both subfilter and up-filter fluxes are positive, which implies an even stronger tilting upshear against the shear that prevails in the background wind. The results suggest that the more organized convection has a pronounced role in setting the meridional wind profile.

c. Coherent, mesoscale circulations across cloud patterns

Here we illustrate the flow associated with the up-filter momentum flux in different cloud patterns. We examine the
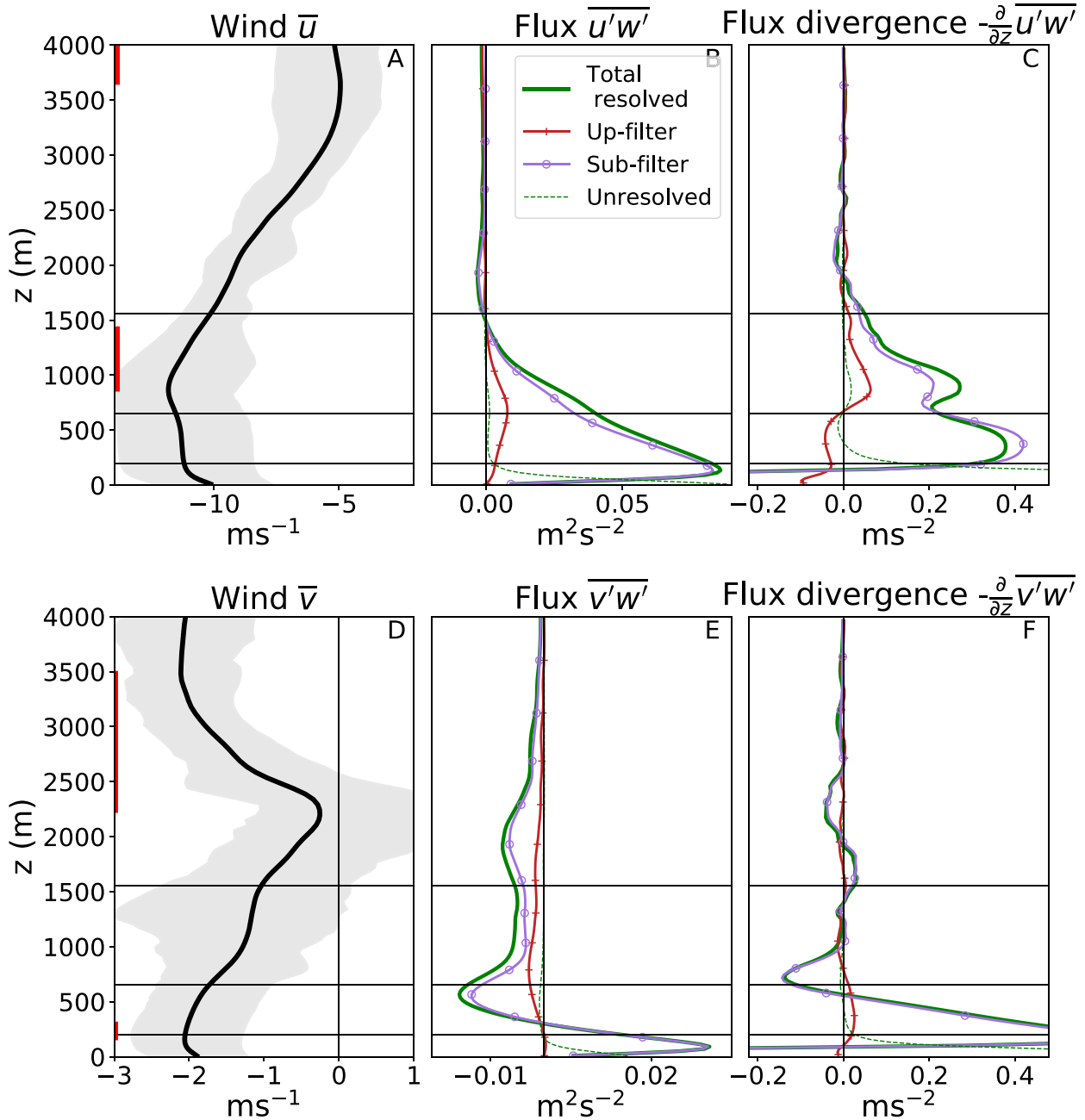
FIG. 10. Vertical profiles for unorganized cases (group 1). (a),(d) Mean zonal and meridional wind and interquartile range. (b),(e) Mean zonal and meridional flux partitioned with a filter of 2 km. (c),(f) Mean zonal and meridional eddy momentum flux divergence. The top, middle, and bottom black horizontal lines mark the mean cloud top, mean cloud base, and 200 m, respectively. The red vertical lines indicate levels of countergradient momentum transport.

flower case at 1000 LT 3 February, which falls in group 3 with an I_{org} value of 0.7 and is depicted in Fig. 2a. Figure 12 shows two vertical cross sections taken at 119.1 km on the *y* axis and at 69.5 km on the *x* axis, representing the decaying phase of a convective system, which started a few hours earlier from a cluster of shallow convective plumes. Those plumes lead to the accumulation of liquid water that spreads around 2 km

(the anvil), and which will become thinner and detached from the convective activity of the boundary layer, but persist for about another hour before dissipating. Rain occurs during the evolution of this system and contributes to its dissipation. The colors represent the zonal and meridional wind anomaly, respectively, while the streamlines are calculated for up-filter wind anomalies corresponding to a filter scale of 15 km. They
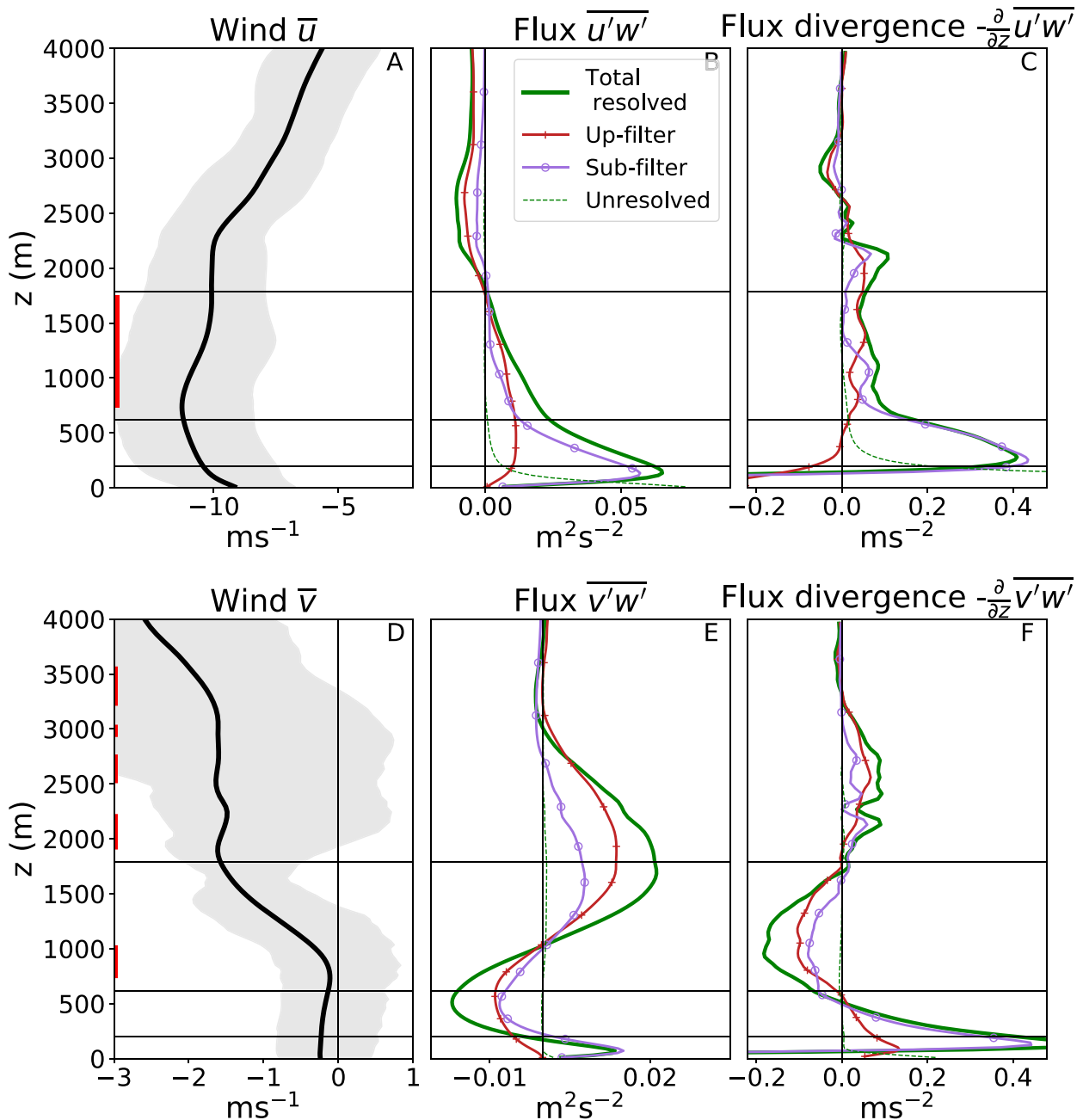
FIG. 11. Vertical profiles for organized cases (group 3). (a),(d) Mean zonal and meridional wind and interquartile range. (b),(e) Mean zonal and meridional flux partitioned with a filter of 2 km. (c),(f) Mean zonal and meridional eddy momentum flux divergence. The top, middle, and bottom black horizontal lines mark the mean cloud top, mean cloud base, and 200 m, respectively. The red vertical lines indicate levels of countergradient momentum transport.

are colored magenta when they are associated with a positive momentum flux, and green for a negative momentum flux.

The wind anomalies highlight a large cold pool, which is symmetrical in the meridional direction but expands more to the west in the zonal direction, influenced by the easterly winds. Winds propagate radially from the center with opposite sign in the anomaly vector and pushing the front. This symmetry explains why cold pools carry momentum fluxes of opposite sign at the two sides of their axis of symmetry (also visible in Figs. 5e,f). The streamlines show the presence of two circulations that expand well beyond the size of the anvil. In both the zonal and meridional direction, Fig. 12 shows two eddies spanning 30–40 km on both sides of the system. The streamlines move upward into the flower, but the horizontal
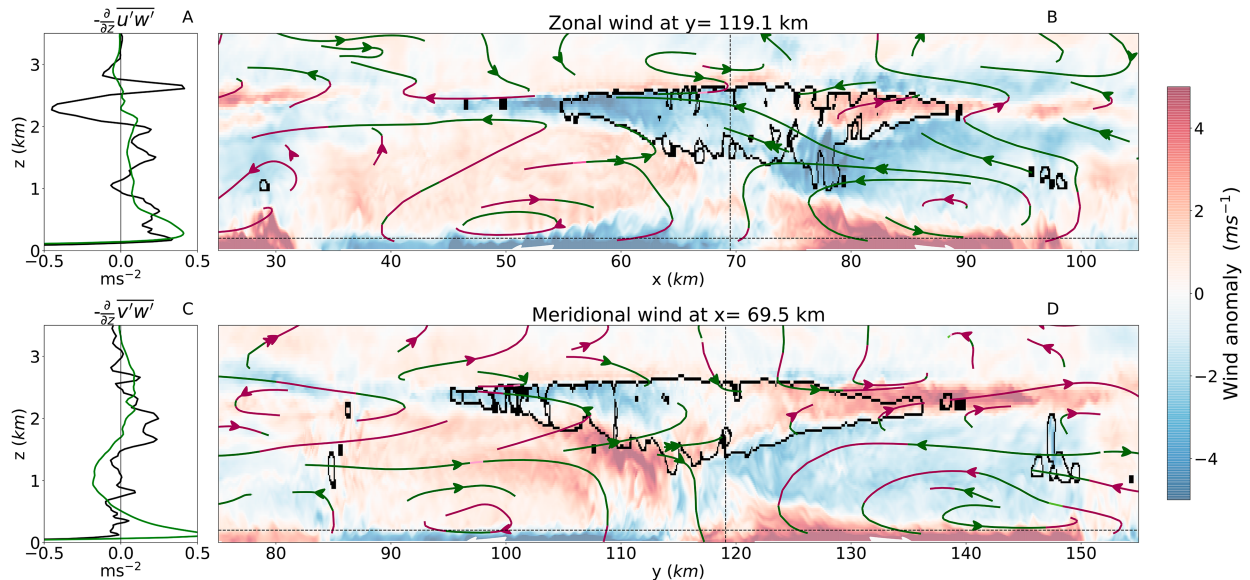
FIG. 12. (a),(c) Mean flux divergence profiles and vertical cross sections of the flower case at 1000 LT 3 Feb. The green profiles in (a) and (c) are (as in Figs. 11c,f) the mean of group 3. The black lines are the slab average for the scene. (b),(d) The contours indicate wind anomaly and the streamlines are the filtered velocity vectors for a filter scale of 15 km. Red streamlines refer to positive momentum flux and green to negative momentum flux.

wind anomaly is only positive in the part of the anvil expanding upstream. For weak background wind and a perfectly symmetric anvil one could expect net zero momentum transport at the anvil level. Nevertheless, the asymmetry of the anvil in the zonal direction (Fig. 12b) produces a strong easterly wind anomaly, large negative momentum fluxes and, as a result, leads to a net acceleration of the easterly flow at the specific time of this flower (black profile in Fig. 12a).

These mesoscale circulations accompanying shallow cloud clusters (titled SMOCS; George et al. 2021a) can expand horizontally for twice the size of the visible anvil and determine the sign and intensity of the domain mean momentum flux. This flower case is a good example of a situation where vertical length scales (e.g., cloud-top height) are not indicative of the size of the eddies nor the scales at which momentum transport occurs.

6. Discussion and conclusions

This study analyses momentum transport from unorganized and nonprecipitating to organized and precipitating shallow convection in simulations on large domains (150×150 km^2) subjected to varying large-scale flow. Its goals are to 1) reveal which scales are contributing to momentum fluxes throughout the boundary layer, 2) study changes in the scale contribution as the cloud field organizes, and 3) study the impact of different scales of momentum transport on the vertical flux divergence.

We simulated 9 days of the EUREC^{4}A campaign with DALES using a horizontal grid spacing of about 100 m, forced with large-scale tendencies from the regional model HARMONIE–AROME. Both DALES and HARMONIE

were run in a climate mode, allowing cloud fields and mesoscale circulations to evolve over multiple days with a wide variety of synoptic conditions. Although the study is not free of limitations, especially with respect to the periodic boundary conditions of DALES, the large spatial domain and the 9-day temporal extent allow us to assess the variability of momentum transport in more complex cloud fields subjected to various dynamical tendencies.

Our results reveal that the momentum flux profile averaged over a large domain is not representative of the flux profile found at individual locations, as the fluxes vary significantly in space and time and even change sign. This variability is observed on submesoscales and mesoscales, with local flux values up to 10 times larger than the domain average. The dominant scales contributing to momentum transport in the cloud layer are notably larger than the dominant scales in the subcloud layer. In the cloud layer scales larger than 2 km contribute between 1% and 80% to the total momentum flux, with large temporal variability that can be explained by the degree of cloud organization. As the cloud field organizes, the contribution of mesoscales to the flux increases. This is true for both the zonal and meridional momentum flux in the cloud layer. For example, when $I_{org} > 0.7$, scales larger than 2 km can contribute to more than 50% of the zonal momentum flux everywhere above cloud base. The meridional momentum flux has an even larger contribution of mesoscales at 200 m and at cloud base, suggesting that horizontal circulations are favored in the crosswind direction.

The mesoscale contribution to heat and moisture fluxes also increases with the degree of organization (see appendix). Mesoscale flux contributions to especially the heat flux are much larger in the subcloud layer and near the surface than

for momentum, because near the surface turbulent wind stresses dominate. However, in the cloud layer the contribution of mesoscales to heat and moisture fluxes is generally smaller or comparable to momentum fluxes. Evidently, horizontal circulations and mesoscale wind inhomogeneity can have scales much larger than the size of a single cloud. The presence of mesoscale circulations with scales on the order of hundreds of kilometers have been observed by George et al. (2021a) during EUREC^{4}A and have been called shallow mesoscale overturning circulations (SMOCS). SMOCS are hypothesized to be internally driven by convection, whose heating anomalies drive ascent that helps aggregate moisture into already moist areas and drives the growth of convective areas to mesoscales (Janssens et al. 2023; Bretherton and Blossey 2017).

The spread in simulated momentum fluxes throughout the 9 days of simulation does not reduce significantly after rescaling the scale contributions to the flux with the cloud-top height. In other words, shallow CMT in complex cloudy atmospheres is, just like deep convection, strongly dependent on accompanying circulations that have scales several times the boundary layer depth. Principally, such circulations should be resolved by models with grid spacing small enough to resolve cloud clusters with length scales of a few kilometers. Thus, the part of the flux that is driven by pressure gradients does not need to be included (anymore) in a mass-flux representation of cloud layer momentum fluxes. To distinguish between momentum transport that should be resolved or parameterized, a vertical length scale cannot be used as, instead, done in current approaches toward scale-adaptive parameterizations of the momentum flux (e.g., Honnert 2019). As the definition of organization is debatable and may be problematic to account for in current models, precipitation might be a good proxy (of organization) for a first step toward better scale-adaptive parameterization.

Several questions remain open in the understanding of mesoscale momentum flux in shallow convective regions. For example, its feedback on the large scale. Also, the role of current shallow convective parameterizations on SMOCS and cloud organization remains largely unexplored, although it is crucial for the improvement of numerical weather predictions. With open boundary conditions, and larger domains, the EUREC^{4}A-MIP will provide coordinated sets of LESs and SRMs to evaluate momentum fluxes in more realistic setups.

APPENDIX

Scales of Heat and Moisture Transport

Figure A1 shows the relative contribution of different scales to the total moisture (red) and heat (brown) flux, together with the zonal (blue) and meridional (green) fluxes. Each column refers to one of the groups based on I_{org} and described in section 4d, whereas each row refers to one height: 200 m, cloud base, and the middle of the cloud layer.

Similar to momentum, I_{org} controls the partitioning of the total heat and moisture fluxes into the various scales. Nevertheless, the shapes of these curves have significant differences, reflecting differences in the processes involved. Shear can be an important driver of momentum flux, while buoyancy is more important for temperature and humidity, which are not influenced by shear (Zhu 2015). At 200 m, especially for group 1 and group 2, the curves of momentum flux grow more rapidly than moisture and heat fluxes. The scales involved for momentum are confined between 0.2 and 2 km. At this height the effect of cold pool is very visible when they occur. Cold pools are more present in organized fields (group 2 and group 3) and they introduce significant contribution of scales larger than 2 km. At 200 m the heat flux (brown) is most dominantly influenced by cold pool dynamics.

At cloud base and in the cloud layer at 1.5 km shear is less strong than at 200 m. Instead, buoyancy becomes the dominant process for the transport of all variables. In the cloud layer heat and moisture fluxes are carried more efficiently by the submesoscales. For unorganized cases (group 1), scales smaller than 1 km carry about 20% more heat and moisture fluxes than momentum fluxes.

Under well-organized conditions (group 3), mesoscale circulations are important for all fluxes as shown by the growth of the curves in Fig. A1i. Here the curves suggest that the heat flux is the least effected by these circulations.
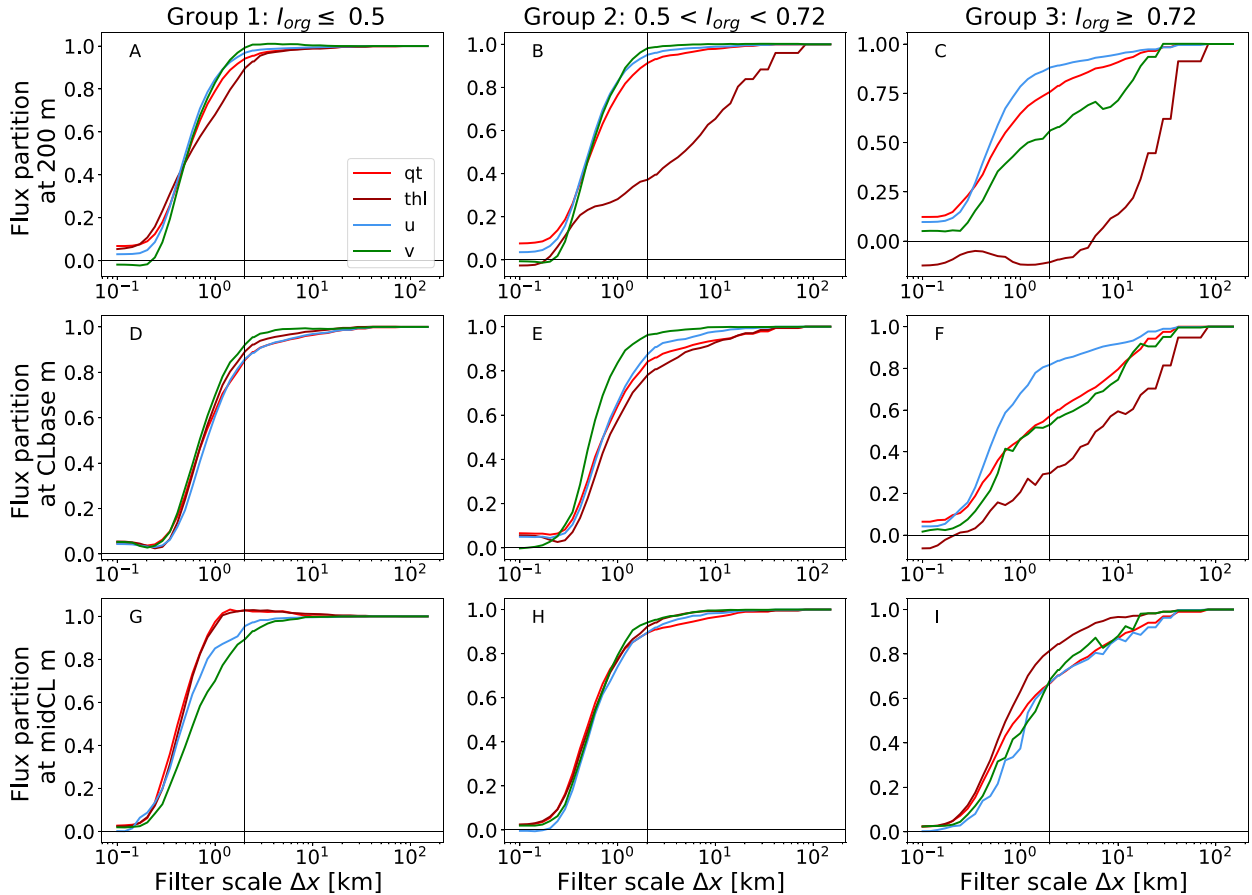
FIG. A1. Partition of the subfilter moisture (red), heat (brown), zonal momentum (blue), and meridional momentum (green) fluxes as a function of the filter scales Δx. The vertical black line denotes $\Delta x = 2$, and each row refers to a different height: (a)–(c) 200 m, (d)–(f) cloud base, and (g)–(i) the middle of the cloud layer. Each column refers to one of the groups based on I_{org}: (a),(d),(g) group 1, (b),(e),(h) group 2, and (c),(f),(i) group 3.

REFERENCES

Badlan, R. L., T. P. Lane, M. W. Moncrieff, and C. Jakob, 2017: Insights into convective momentum transport and its parametrization from idealized simulations of organized convection. *Quart. J. Roy. Meteor. Soc.*, **143**, 2687–2702, https://doi.org/10.1002/qj.3118.

Bengtsson, L., and Coauthors, 2017: The HARMONIE–AROME model configuration in the ALADIN–HIRLAM NWP system. *Mon. Wea. Rev.*, **145**, 1919–1935, https://doi.org/10.1175/MWR-D-16-0417.1.

Bony, S., H. Schulz, J. Vial, and B. Stevens, 2020: Sugar, gravel, fish, and flowers: Dependence of mesoscale patterns of trade-wind clouds on environmental conditions. *Geophys. Res. Lett.*, **47**, e2019GL085988, https://doi.org/10.1029/2019GL085988.

Bretherton, C. S., and P. N. Blossey, 2017: Understanding mesoscale aggregation of shallow cumulus convection using large-eddy simulation. *J. Adv. Model. Earth Syst.*, **9**, 2798–2821, https://doi.org/10.1002/2017MS000981.

Brown, A. R., 1999: Large-eddy simulation and parametrization of the effects of shear on shallow cumulus convection. *Bound.-Layer Meteor.*, **91**, 65–80, https://doi.org/10.1023/A:1001836612775.

Deardorff, J. W., 1980: Stratocumulus-capped mixed layers derived from a three-dimensional model. *Bound.-Layer Meteor.*, **18**, 495–527, https://doi.org/10.1007/BF00119502.

de Rooy, W. C., and Coauthors, 2022: Model development in practice: A comprehensive update to the boundary layer schemes in HARMONIE-AROME cycle 40. *Geosci. Model Dev.*, **15**, 1513–1543, https://doi.org/10.5194/gmd-15-1513-2022.

Dixit, V., L. Nuijens, and K. C. Helfer, 2021: Counter-gradient momentum transport through subtropical shallow convection in ICON-LEM simulations. *J. Adv. Model. Earth Syst.*, **13**, e2020MS002352, https://doi.org/10.1029/2020MS002352.

Dorrestijn, J., D. T. Crommelin, A. P. Siebesma, and H. J. J. Jonker, 2013: Stochastic parameterization of shallow cumulus convection estimated from high-resolution model data. *Theor. Comput. Fluid Dyn.*, **27**, 133–148, https://doi.org/10.1007/s00162-012-0281-y.

Frisch, U., 1995: *Turbulence: The Legacy of A. N. Kolmogorov.* Cambridge University Press, 296 pp., https://doi.org/10.1017/CBO9781139170666.

George, G., B. Stevens, S. Bony, M. Klingebiel, and R. Vogel, 2021a: Observed impact of mesoscale vertical motion on

cloudiness. *J. Atmos. Sci.*, **78**, 2413–2427, https://doi.org/10.1175/JAS-D-20-0335.1.

——, and Coauthors, 2021b: JOANNE: Joint dropsonde Observations of the Atmosphere in tropical North Atlantic mesoscale Environments. *Earth Syst. Sci. Data*, **13**, 5253–5272, https://doi.org/10.5194/essd-13-5253-2021.

Helfer, K. C., L. Nuijens, S. R. de Roode, and A. P. Siebesma, 2020: How wind shear affects trade-wind cumulus convection. *J. Adv. Model. Earth Syst.*, **12**, e2020MS002183, https://doi.org/10.1029/2020MS002183.

——, ——, and V. V. Dixit, 2021: The role of shallow convection in the momentum budget of the trades from large-eddy-simulation hindcasts. *Quart. J. Roy. Meteor. Soc.*, **147**, 2490–2505, https://doi.org/10.1002/qj.4035.

Heus, T., and Coauthors, 2010: Formulation of the Dutch Atmospheric Large-Eddy Simulation (DALES) and overview of its applications. *Geosci. Model Dev.*, **3**, 415–444, https://doi.org/10.5194/gmd-3-415-2010.

Honnert, R., 2019: Grey-zone turbulence in the neutral atmospheric boundary layer. *Bound.-Layer Meteor.*, **170**, 191–204, https://doi.org/10.1007/s10546-018-0394-y.

——, V. Masson, and F. Couvreux, 2011: A diagnostic for evaluating the representation of turbulence in atmospheric models at the kilometric scale. *J. Atmos. Sci.*, **68**, 3112–3131, https://doi.org/10.1175/JAS-D-11-061.1.

Janssens, M., J. V.-G. de Arellano, M. Scheffer, C. Antonissen, A. P. Siebesma, and F. Glassmeier, 2021: Cloud patterns in the trades have four interpretable dimensions. *Geophys. Res. Lett.*, **48**, e2020GL091001, https://doi.org/10.1029/2020GL091001.

——, ——, C. C. van Heerwaarden, S. R. de Roode, A. P. Siebesma, and F. Glassmeier, 2023: Nonprecipitating shallow cumulus convection is intrinsically unstable to length scale growth. *J. Atmos. Sci.*, **80**, 849–870, https://doi.org/10.1175/JAS-D-22-0111.1.

Kershaw, R., and D. Gregory, 1997: Parametrization of momentum transport by convection. I: Theory and cloud modelling results. *Quart. J. Roy. Meteor. Soc.*, **123**, 1133–1151, https://doi.org/10.1002/qj.49712354102.

Khairoutdinov, M., and Y. Kogan, 2000: A new cloud physics parameterization in a large-eddy simulation model of marine stratocumulus. *Mon. Wea. Rev.*, **128**, 229–243, https://doi.org/10.1175/1520-0493(2000)128<0229:ANCPPI>2.0.CO;2.

Larson, V. E., S. Domke, and B. M. Griffin, 2019: Momentum transport in shallow cumulus clouds and its parameterization by higher-order closure. *J. Adv. Model. Earth Syst.*, **11**, 3419–3442, https://doi.org/10.1029/2019MS001743.

Lenderink, G., and A. M. Holtslag, 2004: An updated length-scale formulation for turbulent mixing in clear and cloudy boundary layers. *Quart. J. Roy. Meteor. Soc.*, **130**, 3405–3427, https://doi.org/10.1256/qj.03.117.

Moncrieff, M. W., 1992: Organized convective systems: Archetypal dynamical models, mass and momentum flux theory, and parametrization. *Quart. J. Roy. Meteor. Soc.*, **118**, 819–850, https://doi.org/10.1002/qj.49711850703.

Neggers, R. A. J., 2009: A dual mass flux framework for boundary layer convection. Part II: Clouds. *J. Atmos. Sci.*, **66**, 1489–1506, https://doi.org/10.1175/2008JAS2636.1.

——, J. D. Neelin, and B. Stevens, 2007: Impact mechanisms of shallow cumulus convection on tropical climate dynamics. *J. Climate*, **20**, 2623–2642, https://doi.org/10.1175/JCLI4079.1.

Nuijens, L., A. Savazzi, G. de Boer, P.-E. Brilouet, G. George, M. Lothon, and D. Zhang, 2022: The frictional layer in the observed momentum budget of the trades. *Quart. J. Roy. Meteor. Soc.*, **148**, 3343–3365, https://doi.org/10.1002/qj.4364.

Radtke, J., A. K. Naumann, M. Hagen, and F. Ament, 2022: The relationship between precipitation and its spatial pattern in the trades observed during EUREC^{4}A. *Quart. J. Roy. Meteor. Soc.*, **148**, 1913–1928, https://doi.org/10.1002/qj.4284.

Rio, C., and F. Hourdin, 2008: A thermal plume model for the convective boundary layer: Representation of cumulus clouds. *J. Atmos. Sci.*, **65**, 407–425, https://doi.org/10.1175/2007JAS2256.1.

Schlemmer, L., P. Bechtold, I. Sandu, and M. Ahlgrimm, 2017: Uncertainties related to the representation of momentum transport in shallow convection. *J. Adv. Model. Earth Syst.*, **9**, 1269–1291, https://doi.org/10.1002/2017MS000915.

Schneider, E. K., and R. S. Lindzen, 1976: A discussion of the parameterization of momentum exchange by cumulus convection. *J. Geophys. Res.*, **81**, 3158–3160, https://doi.org/10.1029/JC081i018p03158.

Schulz, H., 2022: C^{3}ONTEXT: A Common Consensus on Convective Organization during the EUREC^{4}A Experiment. *Earth Syst. Sci. Data*, **14**, 1233–1256, https://doi.org/10.5194/essd-14-1233-2022.

Siebesma, A. P., P. M. M. Soares, and J. Teixeira, 2007: A combined eddy-diffusivity mass-flux approach for the convective boundary layer. *J. Atmos. Sci.*, **64**, 1230–1248, https://doi.org/10.1175/JAS3888.1.

Soares, P. M. M., P. M. A. Miranda, A. P. Siebesma, and J. Teixeira, 2004: An eddy-diffusivity/mass-flux parametrization for dry and shallow cumulus convection. *Quart. J. Roy. Meteor. Soc.*, **130**, 3365–3383, https://doi.org/10.1256/qj.03.223.

Stevens, B., and Coauthors, 2021: EUREC^{4}A. *Earth Syst. Sci. Data*, **13**, 4067–4119, https://doi.org/10.5194/essd-13-4067-2021.

Tiedtke, M., 1989: A comprehensive mass flux scheme for cumulus parameterization in large-scale models. *Mon. Wea. Rev.*, **117**, 1779–1800, https://doi.org/10.1175/1520-0493(1989)117<1779:ACMFSF>2.0.CO;2.

Vial, J., and Coauthors, 2019: A new look at the daily cycle of trade wind cumuli. *J. Adv. Model. Earth Syst.*, **11**, 3148–3166, https://doi.org/10.1029/2019MS001746.

——, R. Vogel, and H. Schulz, 2021: On the daily cycle of mesoscale cloud organization in the winter trades. *Quart. J. Roy. Meteor. Soc.*, **147**, 2850–2873, https://doi.org/10.1002/qj.4103.

Vogel, R., H. Konow, H. Schulz, and P. Zuidema, 2021: A climatology of trade-wind cumulus cold pools and their link to mesoscale cloud organization. *Atmos. Chem. Phys.*, **21**, 16 609–16 630, https://doi.org/10.5194/acp-21-16609-2021.

Weger, R. C., J. Lee, T. Zhu, and R. M. Welch, 1992: Clustering, randomness and regularity in cloud fields: 1. Theoretical considerations. *J. Geophys. Res.*, **97**, 20 519–20 536, https://doi.org/10.1029/92JD02038.

Wicker, L. J., and W. C. Skamarock, 2002: Time-splitting methods for elastic models using forward time schemes. *Mon. Wea. Rev.*, **130**, 2088–2097, https://doi.org/10.1175/1520-0493(2002)130<2088:TSMFEM>2.0.CO;2.

Zhu, P., 2015: On the mass-flux representation of vertical transport in moist convection. *J. Atmos. Sci.*, **72**, 4445–4468, https://doi.org/10.1175/JAS-D-14-0332.1.

Zuidema, P., G. Torri, C. Muller, and A. Chandra, 2017: A survey of precipitation-induced atmospheric cold pools over oceans and their interactions with the larger-scale environment. *Surv. Geophys.*, **38**, 1283–1305, https://doi.org/10.1007/s10712-017-9447-x.